

Investigation of Space Interferometer Control Using Imaging Sensor Output Feedback

Victor H. L. Cheng
Optimal Synthesis Inc.
Los Altos, California

Jesse A. Leitner
NASA Goddard Space Flight Center
Greenbelt, Maryland

Abstract

Numerous space interferometry missions are planned for the next decade to verify different enabling technologies towards very-long-baseline interferometry to achieve high-resolution imaging and high-precision measurements. These objectives will require coordinated formations of spacecraft separately carrying optical elements comprising the interferometer. High-precision sensing and control of the spacecraft and the interferometer-component payloads are necessary to deliver sub-wavelength accuracy to achieve the scientific objectives. For these missions, the primary scientific product of interferometer measurements may be the only source of data available at the precision required to maintain the spacecraft and interferometer-component formation. A concept is studied for detecting the interferometer's optical configuration errors based on information extracted from the interferometer sensor output. It enables precision control of the optical components, and, in cases of space interferometers requiring formation flight of spacecraft that comprise the elements of a distributed instrument, it enables the control of the formation-flying vehicles because independent navigation or ranging sensors cannot deliver the high-precision metrology over the entire required geometry.

Since the concept can act on the quality of the interferometer output directly, it can detect errors outside the capability of traditional metrology instruments, and provide the means needed to augment the traditional instrumentation to enable enhanced performance. Specific analyses performed in this study include the application of signal-processing and image-processing techniques to solve the problems of interferometer aperture baseline control, interferometer pointing, and orientation of multiple interferometer aperture pairs.

I. INTRODUCTION

Space-based telescopes such as the Hubble Space Telescope have the advantage of avoiding atmospheric aberration effects affecting ground-based telescopes. To deliver larger apertures without the need of large, single mirrors, interferometry concepts are good candidates for delivering the high resolution with synthetic apertures [1]–[3]. Many of the concepts being developed use separate spacecraft to carry the optical elements to provide the wide separation required to produce the desired aperture. With this approach the resolution of such a synthetic instrument is theoretically unlimited. The current study investigates the control of the spacecraft and their payload optical elements by inferring the required measurement error signals, and in turn, feedback control commands from the interferometric output signals. This control concept can potentially improve the quality of the control beyond what is possible with feedback of metrological measurements alone, and reduce the complexity and cost of the control system by reducing or eliminating the requirements of other sensors and support infrastructure.

NASA missions involving space interferometry currently being planned or considered range from single-spacecraft missions to more sophisticated concepts involving tens of spacecraft. An example of a near-term mission is the Space

Interferometry Mission (SIM) [4][5], which consists of a single spacecraft with three Michelson white-light interferometers [6]–[10]. A far-term example involving multiple spacecraft is the Micro-Arcsecond X-ray Imaging Mission (MAXIM) [11][12], which is a Fizeau X-Ray interferometer concept. The 200-m aperture separation depicted in the MAXIM concept of Figure 1 with 32 collector spacecraft is adequate for detecting targets of angular size of 1 microarcsecond.

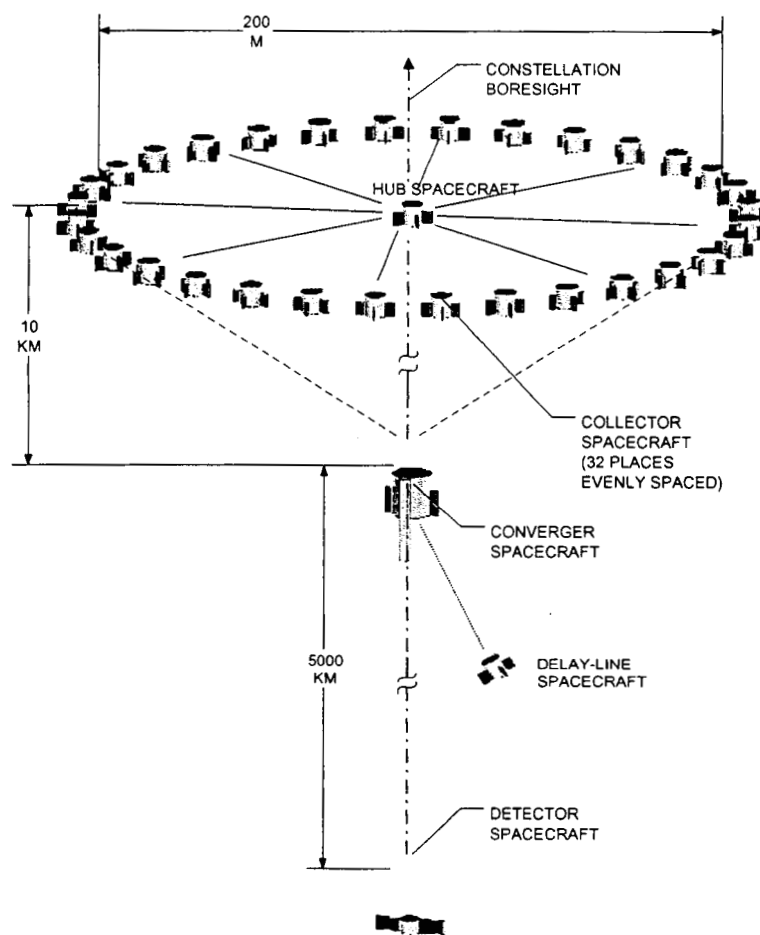


Figure 1. MAXIM Mission Concept (Source [11])

The principal applications of space interferometry are in high-resolution imagery or high-precision astrometric measurements. The current study is based on a generic

interferometer concept for high-resolution imaging with multiple pairs of apertures. Although this generic concept has been motivated by the MAXIM concept in Figure 1, it considers only the simple aspects of the interferometer problem and does not represent any specific mission concept.

Figure 2 shows a general block diagram describing the interferometer feedback control mechanism. The interferometer reacts to the target radiation sources to produce imagery recorded by the imaging sensor. The raw imagery collected by the imaging sensor is typically stored for post-processing to generate the desired scientific output.

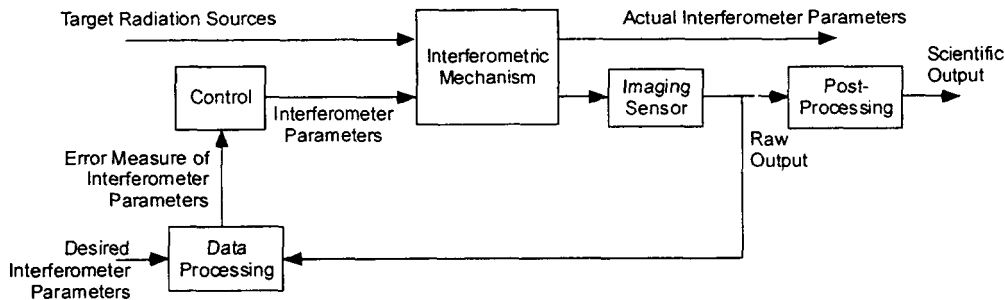


Figure 2. Interferometer Feedback Control Mechanism

Formation of the raw imagery depends on a set of parameters that describe the physical configuration of the interferometer. Metrology instrumentation [13][14] is traditionally used to assure that these parameters are within specification. For the many missions that demand accuracies beyond those available from conventional metrology instrumentation, feedback of information extracted from the raw imagery output may help to reduce or replace the dependence on the metrology instrumentation. Figure 2 suggests that measurements of the actual interferometer parameters may not be directly available for controlling these parameters. In reality, such measurements may be available, but they may not provide the accuracy required for the scientific requirements. The Data Processing subsystem provides the means for assessing errors in the

interferometer parameters based on the raw interferometer output. This produces some pertinent measure of the error parameters for driving the Control subsystem, which in turn generates the necessary control signals for the various optical elements of the interferometer.

The remainder of the paper explores the possibility of extracting useful interferometer parameter information from the imaging sensor output. This is first discussed in the next section for interferometer models with a 1-dimensional (1D) sensor, followed by discussions in Section III on interferometers with a 2D sensor.

II. PLANAR INTERFEROMETER CONFIGURATION WITH 1D SENSOR

II.1 *Sensor Intensity Models*

The first interferometer model contains a sensor to capture the intensity resulting from a point source of radiation. Figure 3 illustrates the interferometer setup with a monochromatic point-source radiation and a single pair of apertures. The apertures denoted by A^+ and A^- may be pinholes or slits in a basic interferometer, or they may represent a pair of collectors in a complex setup such as that of MAXIM (Figure 1). The radiation point source is assumed to be so far away that the wave front is practically planar when it reaches the aperture plane.

Let the image plane defined by the x -axis in this planar model be parallel to the aperture plane, and let O denote the center of the image plane defined relative to the apertures A^+ and A^- . Without loss of generality, let the signal from either A^+ or A^- to O be given by the sinusoid $a \sin \frac{2\pi}{\lambda} ct$, where a is the amplitude, λ is the wavelength of the monochromatic light source, c is the speed of light, and t is time. It follows from

these conditions that the total signal at point P on the imaging plane displaced by distance r from the sensor center O is given by:

$$2a \cos \frac{1}{2} k \frac{rs}{d} \sin k \left(ct + \frac{r^2}{2d} \right) \quad (1)$$

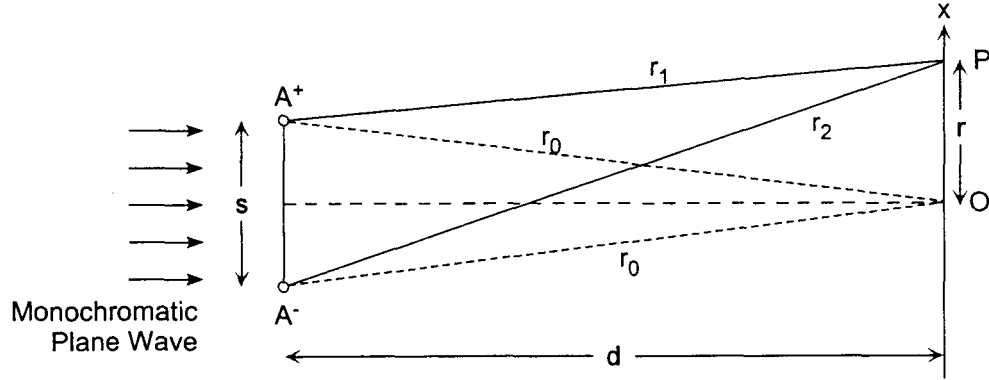


Figure 3. Interferometer with Single Pair of Apertures

This signal is a sinusoid with the same frequency as the one at the center O , with a phase shift of $\frac{kr^2}{2d}$, and amplitude given by

$$2a \cos \frac{1}{2} k \frac{rs}{d} \quad (2)$$

The intensity, or visibility, as detected by an imaging sensor on the imaging plane is proportional to the square of the amplitude of the signal:

$$I(r) \propto 4a^2 \cos^2 \frac{ks}{2d} r = 2a^2 \left(1 + \cos \frac{ks}{d} r \right) \quad (3)$$

This expression describes the point-spread function (PSF) of the basic 2-aperture interferometer.

This model can be extended to the situation where the point source is at an angle ϕ off the centerline of the interferometer. As illustrated in Figure 4, let $a(\phi)$ denote the

effective strength of the signal from the light source. It follows for small ϕ , the signal at the point P would still be a sinusoid with a different phase shift as the one in Eq. (1), and amplitude given by:

$$2a(\phi)\cos\frac{1}{2}k\frac{s}{d}(r-d\cdot\phi) \quad (4)$$

In this case, the intensity, or visibility, as detected by the imaging sensor is:

$$I_{\phi}(r) \propto 4a(\phi)^2 \cos^2 \frac{ks}{2d}(r-d\cdot\phi) = 2a(\phi)^2 \left(1 + \cos \frac{ks}{d}(r-d\cdot\phi) \right) \quad (5)$$

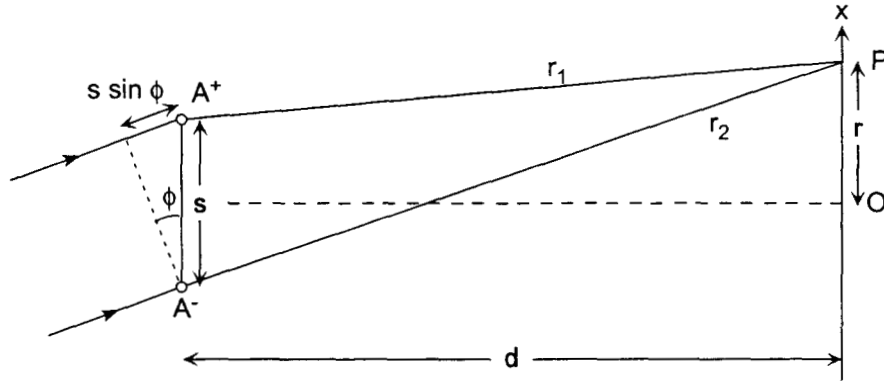


Figure 4. Effect of Off-Axis Light Source

The result in Eq. (5) is also useful for modeling the interferometer output intensity due to an extended source. It is reasonable to assume that the light from different parts of an extended source is not coherent. Under this condition, there will be no interference between the signals originating from different directions, and thus the effect of the intensity of the signals from the different directions will be cumulative. To this end, we consider next an extended source with intensity distribution $E(\phi)$ that varies with direction ϕ to account for the $2a(\phi)^2$ term of Eq. (5). The intensity at P would then be given by:

$$\int E(\phi) \left(1 + \cos \frac{ks}{d} (r - d \cdot \phi) \right) d\phi \quad (6)$$

With a change of variable to replace the distance r with the angle φ that represents the angle of point P off the optical axis as seen from the aperture plane:

$$\frac{r}{d} = \tan \varphi \cong \varphi \quad (7)$$

where the approximation is for small φ , the intensity in Eq. (6) becomes:

$$I(\varphi) = \int E(\phi) (1 + \cos ks(\varphi - \phi)) d\phi \quad (8)$$

By defining h as the impulse response corresponding to the PSF of Eq. (3):

$$h(\varphi) = 1 + \cos ks\varphi \quad (9)$$

the intensity function of Eq. (8) can be expressed as the convolution operation [15]

$$I = E * h \quad (10)$$

This convolution relationship extends directly to the 2D-sensor case.

II.2 Aperture-Baseline Control Problem

The simplest form of the interferometer models as given in Eq. (3) implies that the intensity or visibility at the imaging sensor caused by a distant monochromatic point source resembles a sinusoidal function along the imaging sensor. This observation is useful for detection of any error in controlling the aperture baseline s . Figure 5 illustrates an example of the PSF as the normalized intensity measured with a 512-pixel imaging sensor. The location r on the imaging sensor can be equivalently represented by the angle φ according to the change of variable defined in Eq. (7). Since the intensity function in Eq. (3) indicates that the intensity contains a cosine function in the form of

$$\cos 2\pi \frac{s}{\lambda} \varphi$$

it follows that the intensity exhibits a spatial frequency given by $\frac{s}{\lambda}$. When the baseline s deviates from the desired value \bar{s} , the effect would show up on the measured intensity as an error in the spatial frequency. This error can be detected using the Fast Fourier Transform (FFT). The parameters of the basic interferometer model for generating the PSF in Figure 5 are: baseline $s = 0.01\text{m}$, wavelength $\lambda = 10^{-9}\text{m}$, and pixel resolution $\Delta\varphi = 5 \times 10^{-9}\text{rad}$. Figure 6 shows the magnitude of the FFT (MFT) of the sinusoidal function in Figure 5, with the spatial frequency of the sinusoid showing up as a prominent peak. This spatial frequency can be used to estimate the aperture baseline s , which enables correction of the baseline in a feedback manner.

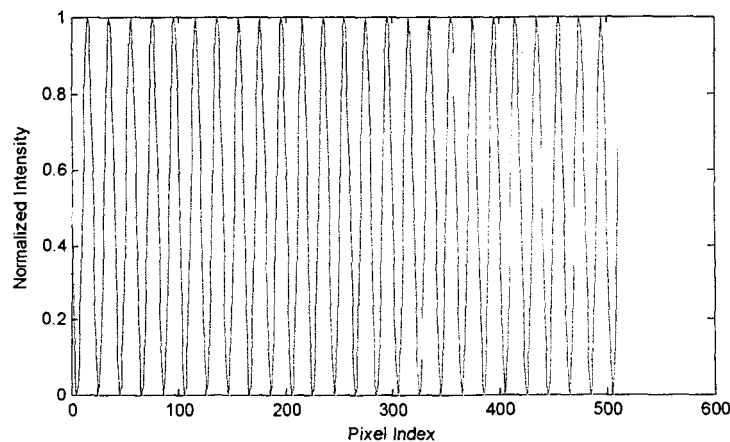


Figure 5. Point-Spread Function Example Formed as Normalized Intensity on the Imaging Sensor by a Distant Monochromatic Point Source

Figure 7 provides some sample results of the baseline estimation and feedback for correction. It can be seen that the estimation and feedback perform reasonably well in correcting for the initial 0.002-m error in the baseline. Since the effect of the baseline

separation error on the spatial frequency is finer than a unit in the spatial frequency index of the MFT in Figure 6, estimation of the peak has to achieve sub-unit accuracy on the spatial frequency axis. This is obtained through peak detection of spline-fitted data.

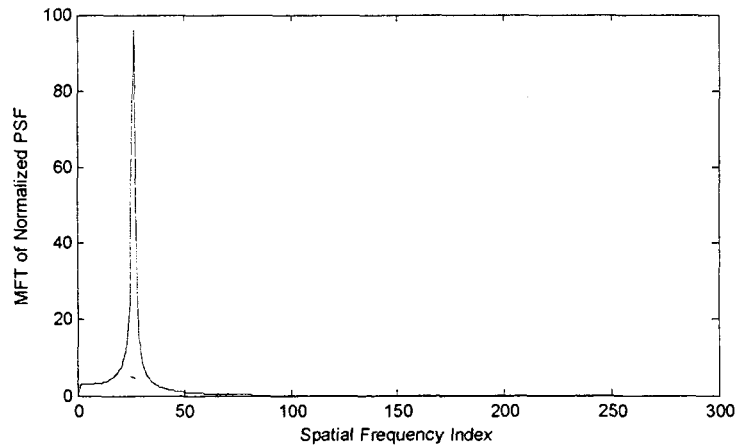


Figure 6. Magnitude of FFT of Intensity Profile from Figure 5 with DC Value Removed

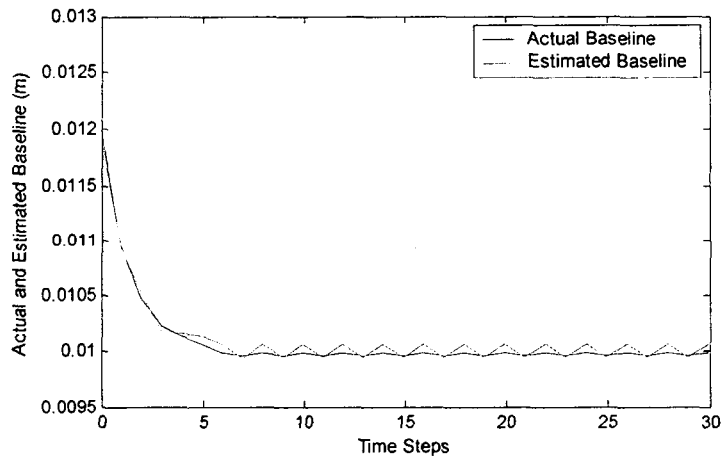


Figure 7. Aperture-Baseline Estimation and Feedback Results

The evaluation example above is next extended to include the effect of noise on the sensor measurements. In all the cases studied, noise is modeled as a Gaussian white noise distribution with zero mean, and a standard deviation σ equal to 20% of the

dynamic range of the original, noiseless measurements. An example of the noisy measurement is given in Figure 8. The results of the estimation and feedback of the aperture baseline based on noisy intensity measurements are given in Figure 9. The effect of the noise on the final response is obvious, but it is evident that the effects are not detrimental.

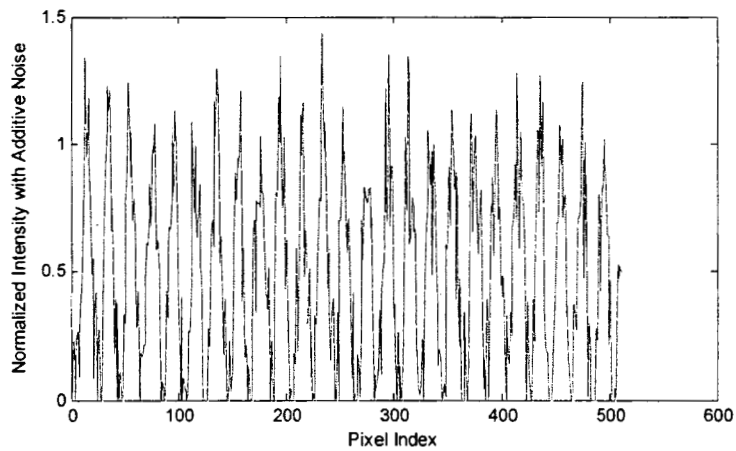


Figure 8. Intensity Profile with Noise

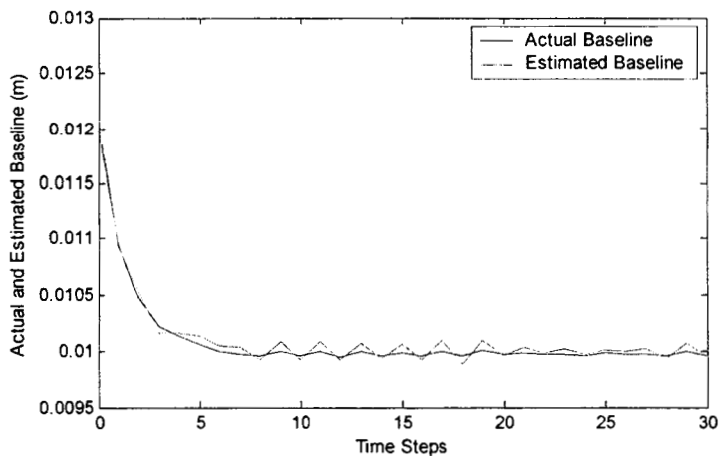


Figure 9. Aperture-Baseline Estimation and Feedback Results with Noise

II.3 Interferometer Pointing Problem

The intensity value given in Eq. (5) describes the effect of a point source at an angle ϕ from the centerline of the interferometer. The resulting intensity profile can be used to study the control of the orientation of the interferometer, assuming the whole interferometer can be maneuvered as a single system. The next example considers the control of the interferometer to point directly at a distant point source, i.e. $\phi = 0^\circ$. Controlling it to align with any other nonzero ϕ is a simple extension of this example.

The approach to controlling the pointing of the interferometer is based on the observation that the intensity profile of the interferometer as given in Figure 5 contains a cosine function centered about the origin of the sensor. Any nonzero slope of the intensity function at the origin can be used to infer a pointing error. The intensity slope about the origin of the imaging sensor is estimated by fitting a linear line segment through the neighboring data using a least-square criterion. In this example, the interferometer is subjected to an initial pointing error equal to 5 times the pixel resolution, i.e. approximately 5.2 marcsec. Figure 10 illustrates the estimated error slope as a result of the estimation procedure and iterative feedback correction. Figure 11 shows the corresponding pointing error, which demonstrates the efficacy of the combined estimation and feedback procedure.

This evaluation example is next studied under the effect of sensor noise. Initial results confirm the undesirable effect of the differentiation operation for estimating the intensity slope, which tends to amplify the effect of noise. To help alleviate the effect of noise, an ensemble of 10 independent intensity profiles is taken at each iteration to produce an average profile, which is then used for the intensity-slope estimation and

pointing correction. The averaging of the ensemble effectively reduces the standard deviation of the noise. The resulting pointing error is given in Figure 12, which shows more acceptable performance than the case without noise averaging, which is not shown here due to space limitation.

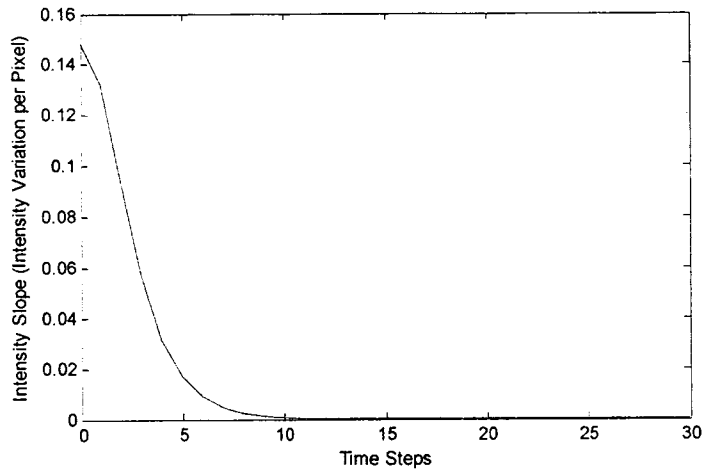


Figure 10. Estimated Intensity Slope at Center of Sensor

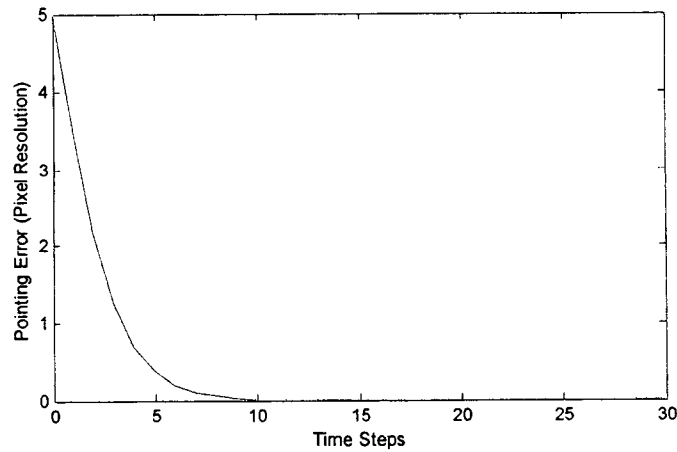


Figure 11. Pointing Error with Feedback Correction

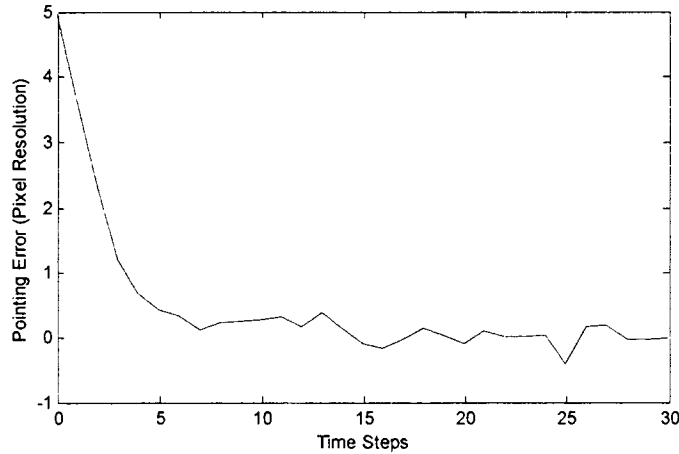


Figure 12. Pointing Error with Averaged Sensor Noise

II.4 Combined Aperture-Baseline Control and Interferometer-Pointing Problem

The next example combines the two preceding problems: aperture baseline error and interferometer pointing error. The interferometer simulation is subjected to both of these errors, and the estimation and feedback algorithms from Sections II.2 and II.3 are simultaneously applied. The aperture-baseline results are similar to those shown in Figure 7, and the estimated intensity slope and pointing error are similar to the results in Figure 10 and Figure 11, respectively; hence these plots are omitted here. These results illustrate the capability to isolate the effects due to the individual parameter errors to support decoupled corrective actions. Repeating this analysis with sensor noise again produces results similar to those from the individual cases.

II.5 Aperture-Baseline Control Problem with Extended Source

The formulation of the interferometer model in Eqs. (8) and (10) is next used to study the effect of an extended source. Figure 13 contains an example of the intensity profile of an artificial extended source, formed by adding a small sinusoidal variation to a

constant, unit intensity. Several widths of the extended source are considered for the examples: 15, 31, and 51 pixels. These widths are chosen to study their effects on the interferometer model used in the analyses, where the PSF has a spatial period of about 25.6 pixels.

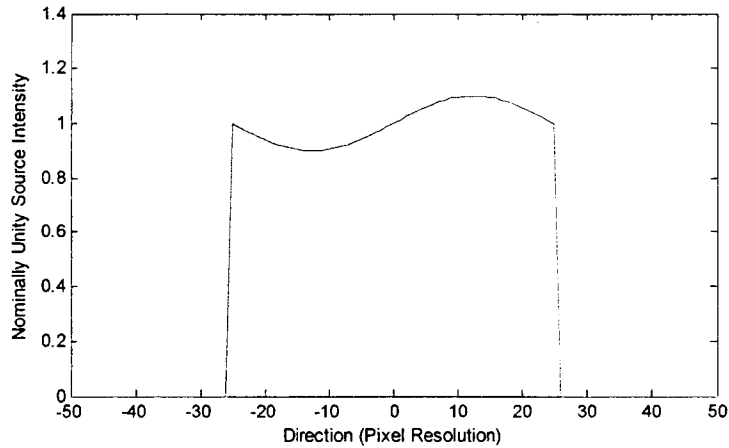


Figure 13. Intensity of Artificial Extended Source

Figure 14 shows the interferometer output intensities as the result of the 31-pixel source. The intensities of the other two cases look similar, albeit with different magnitude values. Although they are not necessarily simple cosine functions as in the impulse response, they nevertheless show that the periodicity of the impulse response is still prominent.

The same aperture-baseline estimation and feedback algorithm described in Section II.2 is applied to correct for the baseline error, using the interferometer output intensity caused by the extended sources. The results with any of the three extended source are very similar to those obtained for the point-source case in Section II.2, including the cases with sensor noise present. The reason is that the frequency of the

cosine function in the impulse response is still the most prominent frequency in the intensity signal from the extended source.

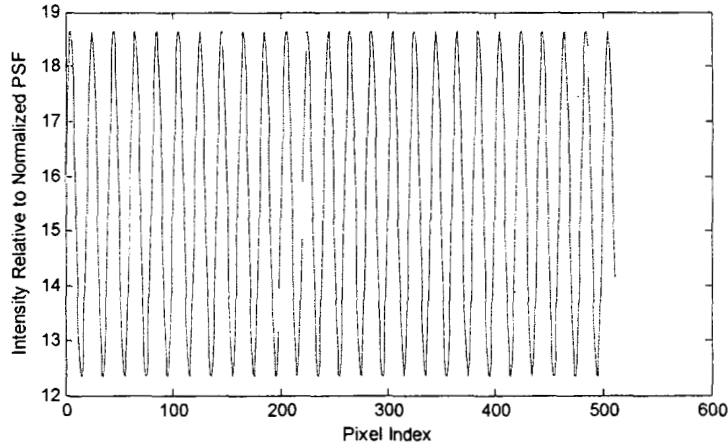


Figure 14. Intensity Profile with 31-Pixel Source

III. INTERFEROMETER CONFIGURATION WITH 2D SENSOR

III.1 Sensor Intensity Models

Still considering a single pair of apertures, we next study the sensor output on the image plane off the x -axis as in Figure 15. Consider a point $P = (x, y)$ on the image plane, with r and θ denoting its polar representation.

It follows from these conditions that the total signal at the point P is again given by

$$2a \cos \frac{1}{2} k \frac{rs \cos \theta}{d} \sin k \left(ct + \frac{r^2}{2d} \right) \quad (11)$$

The resulting signal in Eq. (11) is again a sinusoid with the same frequency and phase shift as the one in Eq. (1). The important conclusion here is that the phase shift depends only on the distance r , but is otherwise independent of the angle θ . This property makes it possible to arrive at the model with multiple pairs of apertures

discussed below by superimposing the respective signals. The amplitude of the sinusoid, on the other hand, is a function of both r and θ , as given by

$$2a \cos \frac{1}{2} k \frac{rs \cos \theta}{d} \quad (12)$$

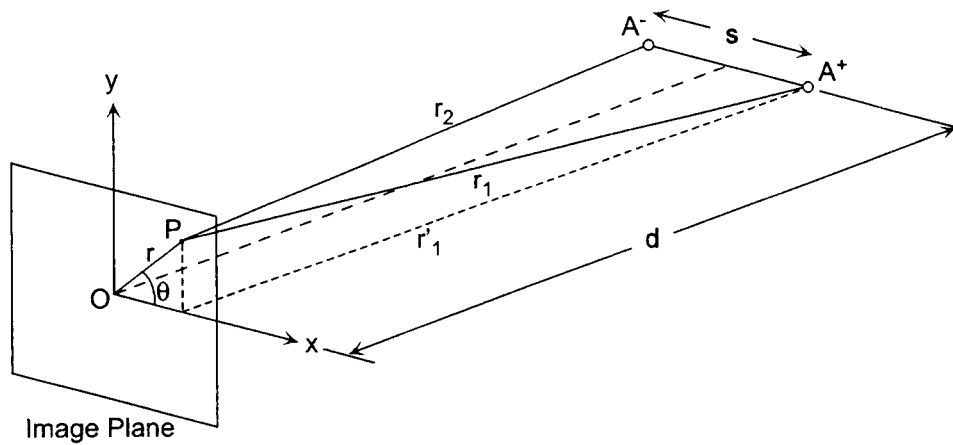


Figure 15. 2D Image Plane for Interferometer with Single Pair of Apertures

The interferometer situation with multiple pairs of apertures, namely N , is shown in Figure 16. Let θ_i denote the angle made by the i^{th} pair with respect to the plane defined by the x -axis. This convention assumes $\theta_0 = 0^\circ$.

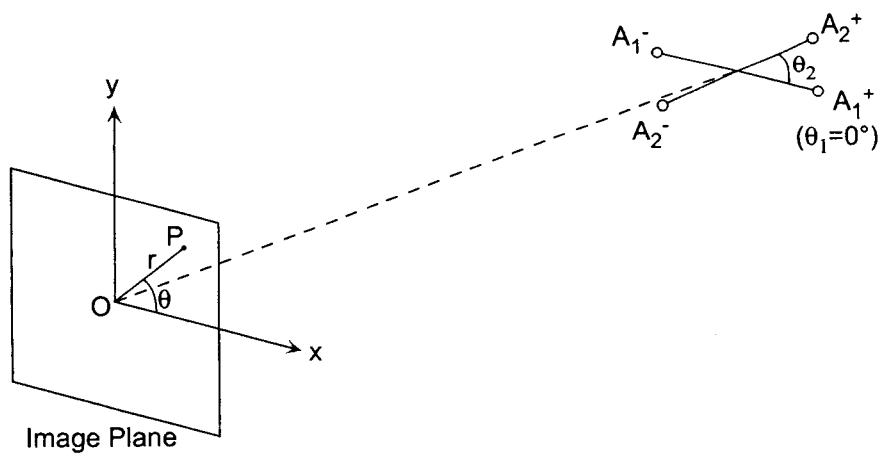


Figure 16. Interferometer with Multiple Pairs of Apertures

Since the total signal at a point on the image plane from a pair of apertures experiences a phase shift that depends only on r but not on θ , the amplitudes of the signals from the individual aperture pairs can be directly summed. From Eq. (11), the total signal at the point $P = (x, y) = (r \cos \theta, r \sin \theta)$ on the image plane is given by:

$$\sum_{i=1}^N 2a \cos \frac{1}{2} k \frac{rs \cos(\theta - \theta_i)}{d} \sin k \left(ct + \frac{r^2}{2d} \right) \quad (13)$$

This is a sinusoid with amplitude

$$\sum_{i=1}^N 2a \cos \frac{1}{2} k \frac{rs \cos(\theta - \theta_i)}{d} \quad (14)$$

and its intensity or visibility is proportional to

$$\left(\sum_{i=1}^N 2a \cos \frac{1}{2} k \frac{rs \cos(\theta - \theta_i)}{d} \right)^2 \quad (15)$$

III.2 Aperture-Pair Orientation Problem with One Pair of Apertures

Figure 17 depicts the intensity maps as measured by the 2D imaging sensor with one pair of apertures, computed according to Eq. (12). The objective of this analysis is to infer any orientation error of the aperture pair from the intensity map so that the error can be corrected.

Let $\theta = 0^\circ$ be the nominal orientation desired for the pair of apertures. The arrow in Figure 18 indicates this reference direction. It can be observed that the spatial frequency along this direction should be higher than those along neighboring directions within a sector as illustrated in Figure 18. The principal spatial frequencies along these directions are determined according to the technique used in Section II.2. As expected, the spatial frequency depicted in Figure 19 peaks in the nominal direction.

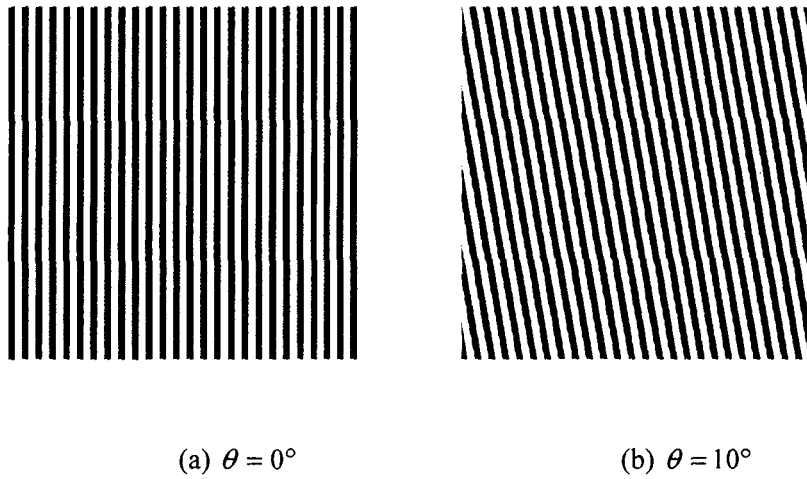


Figure 17. 2D Intensity Maps with 1 Pair of Apertures

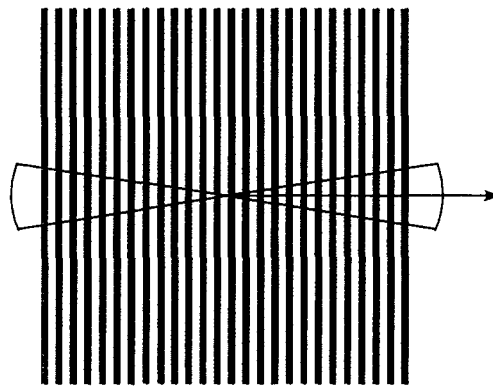


Figure 18. Sector of Radial Search Directions to Determine Spatial Frequencies

If the aperture pair has an error in its orientation, then the spatial frequency plot in Figure 19 would be shifted sideways accordingly. By searching for the peak of this spatial frequency plot, the orientation error can be estimated. Figure 20 shows the results in both estimated and actual orientation error due to an initial orientation error of 10° . The results show that the estimation performs very well in reproducing the error. Figure 21 shows the results from the same situation, except that the sensor is subject to noise.

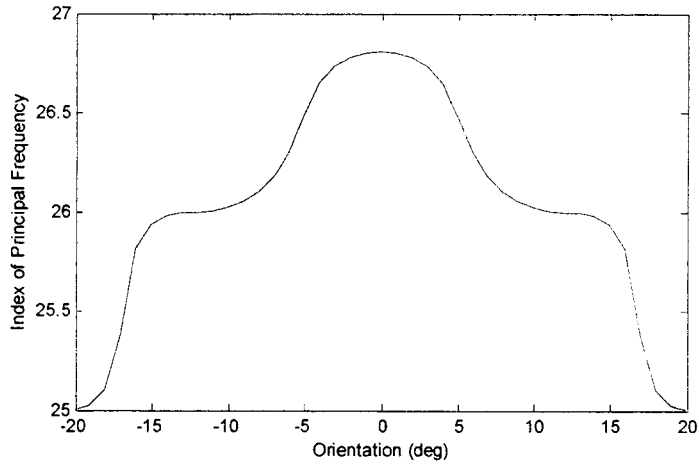


Figure 19. Variation of Spatial Frequency as a Function of Orientation

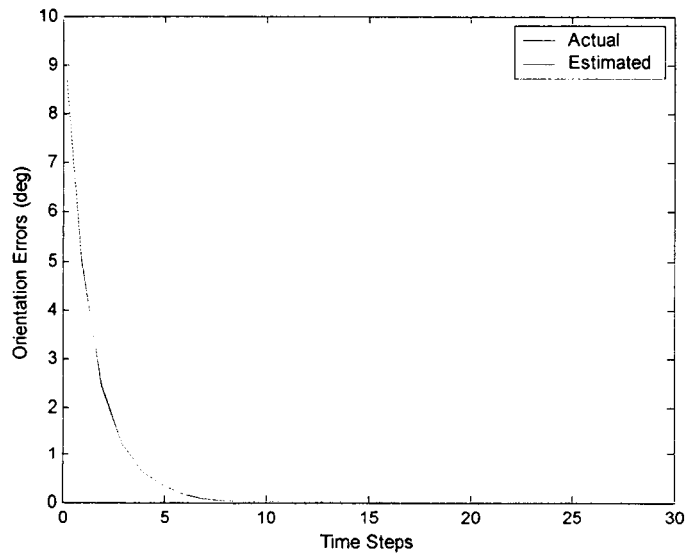


Figure 20. Orientation Error for One Pair of Apertures

III.3 Aperture-Pair Orientation Problem with Two Pairs of Apertures

The problem with two pairs of apertures is an extension of the problem in the previous section. Figure 22 contains two example intensity maps: the first one with nominal orientations given by $(\theta_1, \theta_2) = (0^\circ, 90^\circ)$, and the second one given by

$(\theta_1, \theta_2) = (0^\circ, 80^\circ)$. Comparing these two intensity maps, it is interesting to note that change in the orientation $\theta_2 = 90^\circ$ has resulted in a change of the fringe pattern along the 0° direction, whereas the orientation $\theta_1 = 0^\circ$ is reflected in the fringe pattern along the 90° direction. This orthogonal relationship needs to be taken into account when estimating the orientation of multiple pairs of apertures.

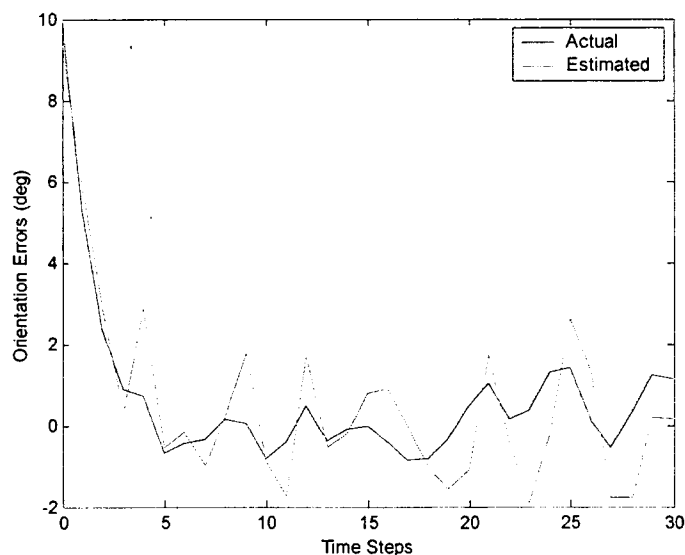
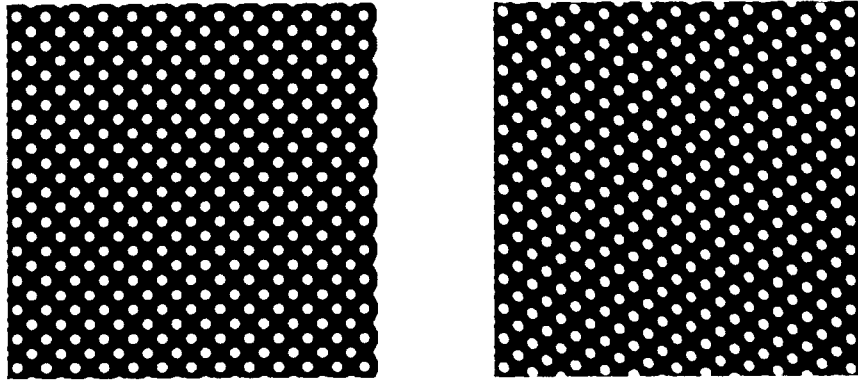


Figure 21. Orientation Error for One Pair of Apertures with Sensor Noise

The approach used for estimating the orientation errors for two pairs of apertures is essentially the same as that for a single pair, except that the sector in which the radial directions would give useful spatial-frequency information is much more restricted.

Figure 23 shows the estimation and feedback results with initial orientation errors of $(-1^\circ, +2^\circ)$. Analysis under the influence of sensor noise shows results similar to those in Figure 21.



(a) $(\theta_1, \theta_2) = (0^\circ, 90^\circ)$

(b) $(\theta_1, \theta_2) = (0^\circ, 80^\circ)$

Figure 22. 2D Intensity Maps with 2 Pairs of Apertures

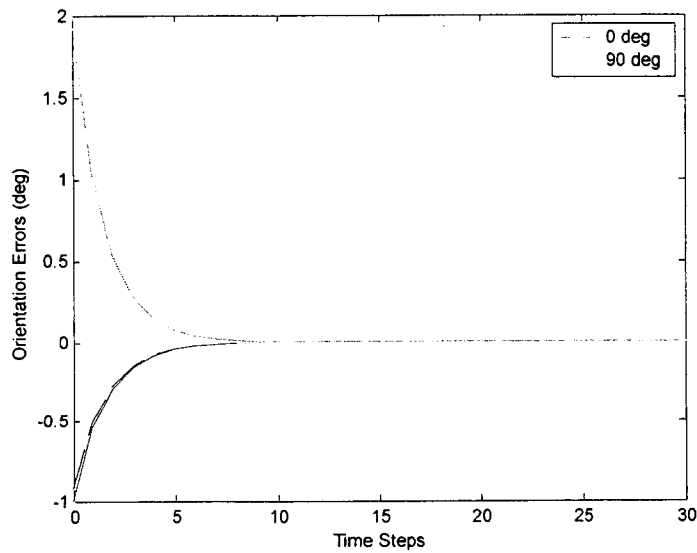


Figure 23. Orientation Errors for Two Pairs of Apertures

III.4 Aperture-Pair Orientation Problem with Three Pairs of Apertures

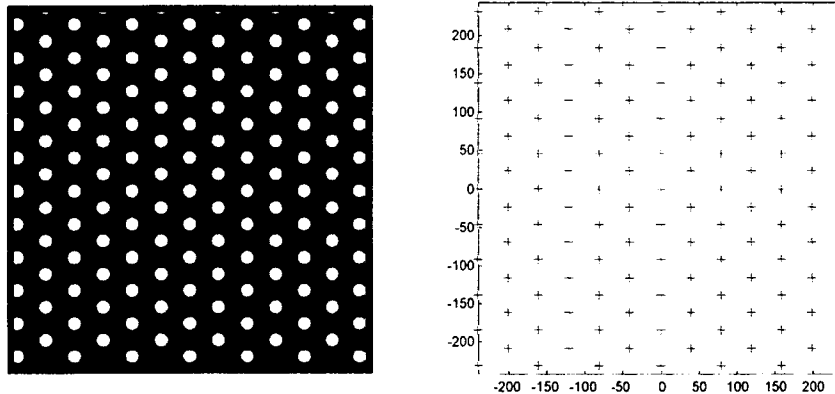
The problem with three pairs of apertures was expected to be similar to that with two pairs as in previous section. The search sectors were expected to be even more

restricted than the previous case. However, due to the more complex fringe patterns, initial analyses showed that it was extremely difficult to obtain sufficiently good spatial frequency information along these directions for estimating the orientation errors. Hence it became necessary to look for a new approach for estimating the orientation errors.

Instead of just scanning the fringe patterns along selected radial directions, a new approach was designed to take advantage of the fringe patterns throughout the intensity map. The Hough transform [16][17] has the potential for identifying groups of points that lie in straight lines, and this property can be exploited to estimate the orientation of the intensity peaks that form the fringe patterns. A procedure for determining the directions of these patterns is as follows:

- (i) With the center region of the impulse response containing an intensity peak as the template, perform a correlation with the whole intensity map. (Figure 24(a))
- (ii) Identify the peaks from the correlation results. (Figure 24(b))
- (iii) Perform Hough transform on the identified peaks.
- (iv) Based on the Hough transform, detect collinear points from the identified peaks.
- (v) Collect directions of the collinear points and use them to estimate the orientation of the aperture pairs as in the previous problem, where the orthogonal relationship between the fringe pattern and the aperture-pair orientation still holds.

The reason behind the correlation operation in steps (i) and (ii) is to anticipate the situation of extended sources that include complex intensity profiles. The correlation will help to create correlation peaks that better resemble those of the PSF.



(a) Correlation Results

(b) Identified Peaks from Correlation

Figure 24. Processing of Data for Hough Transform

Analysis results with initial orientation errors of $(-2^\circ, +5^\circ, +3^\circ)$ shown in Figure 25 indicate that the overall performance was quite good. Figure 26 shows the corresponding estimated orientation errors, which incidentally shows that the initial estimate for the first orientation was rather inadequate, and the initial estimates of the other two orientations were not totally accurate either. These results suggest that the fringe patterns, resulting as the combination of nonlinear signals, may produce pattern orientations not exactly orthogonal to the aperture-pair orientations when the patterns are irregular. Nevertheless, as the second and third orientations converge, the estimate for the first orientation improves and ultimately all three orientation errors converge to zero.

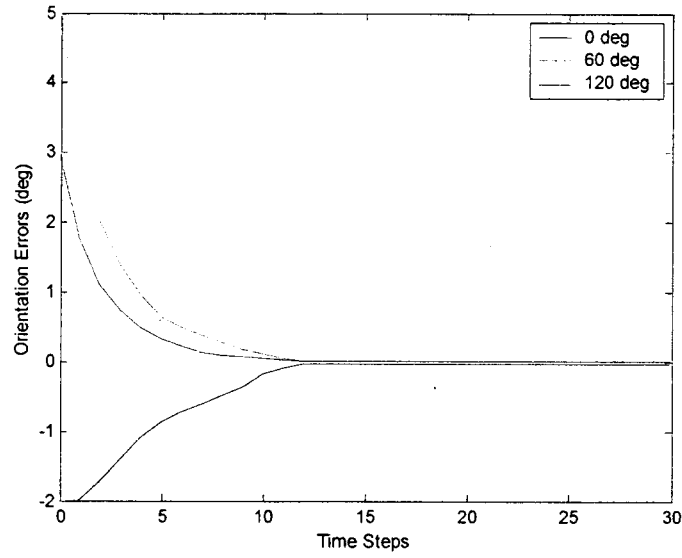


Figure 25. Orientation Errors for Three Pairs of Apertures

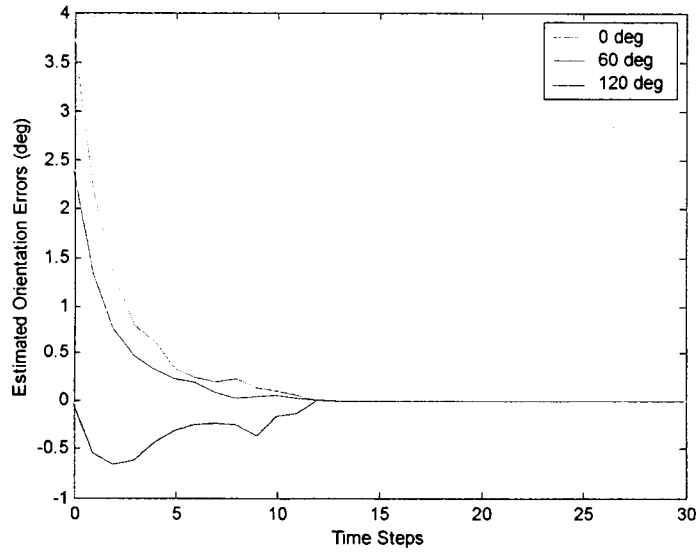
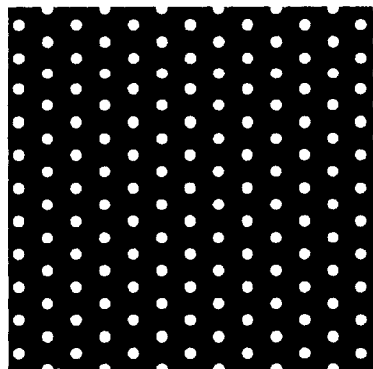


Figure 26. Estimated Orientation Errors for Three Pairs of Apertures

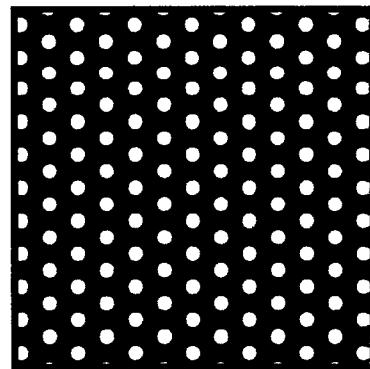
III.5 Aperture-Pair Orientation Problem with Extended Sources

The formulation of the interferometer model for an extended source discussed in Section II.1 is extended to study the effect of an extended source for the 2D sensor. For this analysis, the intensity map of the extended source is modeled as a disk with small variation superimposed over a constant intensity. The small variation decreases as a cosine function from the center of the disk radially towards the edge. The peak variation at the center is 10% of the constant intensity value. Similar to the 1D sensor case, three sizes of extended source are considered, with disk diameters of 15 pixels, 31 pixels and 51 pixels.

Figure 27(a) contains the intensity map measured by the 2D sensor for the 15-pixel-diameter source, and part (b) contains the corresponding correlation results. The feedback and estimation results are almost identical to the point-source results in the Figure 25 and Figure 26, and are therefore omitted. Analyses with the two other extended sources produce similar results.



(a) Intensity Map



(b) Correlation Results

Figure 27. Intensity Map and Correlation Results for 15-Pixel-Diameter Source

Finally, the analyses for the 15-pixel-diameter extended source are repeated with sensor noise present. The feedback and estimation results are provided in Figure 28 and Figure 29.

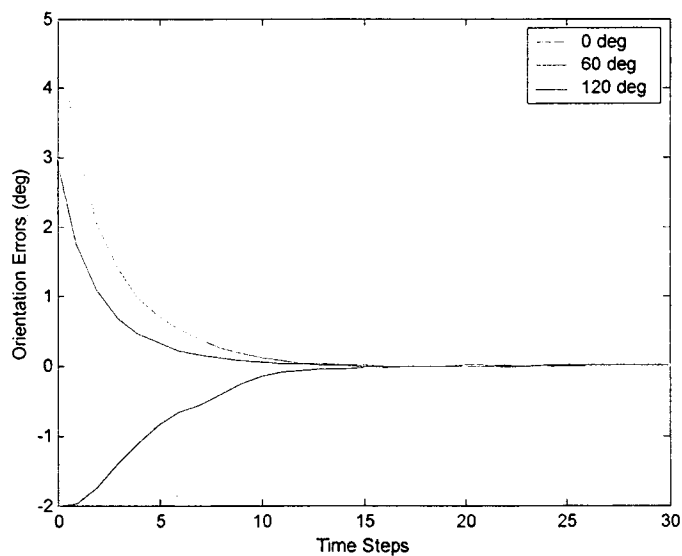


Figure 28. Orientation Errors with 15-Pixel-Diameter Source and Sensor Noise

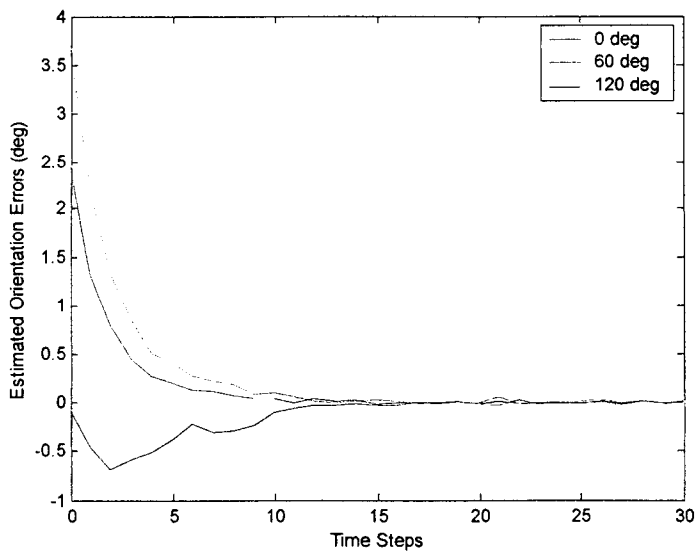


Figure 29. Estimated Orientation Errors with 15-Pixel-Diameter Source and Sensor Noise

IV. CONCLUDING REMARKS

An online control concept for correcting optical alignment errors in imaging interferometer applications has been suggested and analyzed with several simulated examples. The concept is useful for detecting the interferometer's optical configuration errors based on information extracted from the interferometer sensor output. It enables precision control of the optical components, and in cases of space interferometers requiring formation flight of spacecraft carrying the optical components as payloads, it enables the control of the formation-flying vehicles. Since the concept can act on the quality of the interferometer output directly, it has the potential for detecting errors outside the capability of traditional metrology instruments, and the possibility of augmenting the traditional instrumentation for enhanced performance.

Several examples matched with data-processing techniques have been studied to assess the viability of this concept. Signal processing based on frequency domain analysis has been successfully demonstrated to analyze and correct for aperture baseline errors. This technique is particularly valuable in situations where the characteristic is more prominent in the frequency domain than in the spatial domain. Noise is often easier to deal with when one needs to work with only a narrow band in the frequency domain to extract the pertinent information.

Signal processing in the spatial domain has been applied to study the correction of the interferometer's pointing error. This method is useful when it is easy to discern the signal properties directly from the original output signal.

An image-processing technique based on the Hough transform has been successfully applied to analyze and correct for the orientation errors of aperture pairs

making up the interferometer. It has performed nicely in making good use of the information over the whole sensor to assess the orientation errors.

The examples used in this initial study are relatively simplistic and do not adequately characterize the difficult control problems associated with a realistic mission scenario involving all degrees of freedom for controlling all the optical elements. The techniques presented here do not involve explicit wavefront estimation, whereas future research will consider the use of such procedures to identify the errors associated with all the degrees of freedom that may introduce errors into the interferometer system.

V. ACKNOWLEDGMENT

The authors thank Prof. Webster Cash and Mr. Randy McEntaffer from the University of Colorado for providing valuable insight in the MAXIM concept and modeling information. This work was supported in part by NASA under Contract No. NAS5-01184.

REFERENCES

- [1] P. R. Lawson (Ed.), *Selected Papers on Long Baseline Stellar Interferometry*, SPIE Milestone Series, Vol. MS 139, SPIE, 1997.
- [2] R. D. Reasenberg, *Astronomical Interferometry*, Proceedings of SPIE, Vol. 3350, Kona, HI, March 20–24, 1998.
- [3] R. D. Reasenberg, *Spaceborne Interferometry II*, Proceedings of SPIE, Vol. 2477, Orlando, FL, April 19–20, 1995.
- [4] R. A. Laskin, "The Space Interferometry Mission (SIM) — Meeting the Technology Challenge," *Photonics for Space and Enhanced Radiation Environments Conference (PSERE)*, Paper No. 3872-13, European Optical Society/SPIE Symposium on Remote Sensing, Florence, Italy, September 1999.
- [5] *SIM — Space Interferometry Mission*, website <http://sim.jpl.nasa.gov/>.

- [6] A. A. Michelson, "On the Application of Interference Methods to Astronomical Measurements," *London, Edinburgh and Dublin Philosophical Magazine and Journal of Science*, Vol. 30, pp. 1–21, July 1890.
- [7] A. A. Michelson, "Visibility of Interference-Fringes in the Focus of a Telescope," *London, Edinburgh and Dublin Philosophical Magazine and Journal of Science*, Vol. 31, pp. 256–259, 1891.
- [8] A. A. Michelson, "Measurement of Jupiter's Satellites by Interference," *Nature*, Vol. 45, pp. 160–161, December 17, 1891.
- [9] A. A. Michelson, "On the Application of Interference Methods to Astronomical Measurements," *Astrophysical Journal*, Vol. 51, No. 5, pp. 257–262, June 1920.
- [10] A. A. Michelson and F. G. Pease, "Measurement of the Diameter of α Orionis with the Interferometer," *Astrophysical Journal*, Vol. 53, pp. 249–259, 1921.
- [11] *MAXIM — Micro-Arcsecond X-ray Imaging Mission*, website <http://maxim.gsfc.nasa.gov/>.
- [12] W. Cash, "MAXIM Preliminary Design," *NAIC Report*, NASA Institute for Advanced Concepts, August 2000.
- [13] Y. Gürsel, "Metrology for Spatial Interferometry," *Amplitude and Intensity Spatial Interferometry II*, SPIE Proceedings, Vol. 2200, Kona, HI, March 15–16, 1994, pp. 27–34.
- [14] Y. Gürsel, "Metrology for Spatial Interferometry II," *Spaceborne Interferometry II*, SPIE Proceedings, Vol. 2477, Orlando, FL, April 19–20, 1995, pp. 240–258.
- [15] F. T. S. Yu and I. C. Khoo, *Principles of Optical Engineering*, Wiley, 1990.
- [16] W. K. Pratt, *Digital Image Processing*, Wiley, 1991.
- [17] G. X. Ritter and J. N. Wilson, *Handbook of Computer Vision Algorithms in Image Algebra*, CRC Press, 1996.